1 **OptoRheo: Simultaneous *in situ* micro-mechanical sensing and**

2 **imaging of live 3D biological systems**.

3 **Authors:** Tania Mendonca[1], Katarzyna Lis-Slimak[2], Andrew B. Matheson[3], Matthew G.

4 Smith[4], Akosua B. Anane-Adjei[5], Jennifer C. Ashworth[6,7], Robert Cavanagh[5], Lynn

5 Paterson[3], Paul A. Dalgarno[3], Cameron Alexander[5], Manlio Tassieri[4], Catherine L. R.

6 Merry[2] and Amanda J. Wright[1]

7

8 [1] Optics and Photonics Research Group, Faculty of Engineering, University of Nottingham,

9 Nottingham, NG7 2RD, UK

10 [2] Stem Cell Glycobiology Group, Nottingham Biodiscovery Institute, School of Medicine,

11 University of Nottingham, Nottingham, NG7 2RD, UK

12 [3] Institute of Biological Chemistry, Biophysics and Bioengineering, School of Engineering

13 and Physical Sciences, Heriot Watt University, Edinburgh, EH14 4AS, UK

14 [4] Division of Biomedical Engineering, James Watt School of Engineering, University of

15 Glasgow, Glasgow, G12 8LT, UK

16 [5] School of Pharmacy, University of Nottingham, Nottingham NG7 2RD, UK

17 [6] School of Veterinary Medicine & Science, University of Nottingham, Sutton Bonington

18 Campus, Leicestershire, LE12 5RD, UK

19 [7] Nottingham Biodiscovery Institute, School of Medicine, University of Nottingham,

20 Nottingham, NG7 2RD, UK

21

22 **Abstract**

23 Biomechanical cues from the extracellular matrix (ECM) are essential for directing many

24 cellular processes, from normal development and repair, to disease progression. To better

25 understand cell-matrix interactions, we have developed a new instrument named 'OptoRheo'

26 that combines light sheet fluorescence microscopy with particle tracking microrheology.

27 OptoRheo lets us image cells in 3D as they proliferate over several days while

28   simultaneously sensing the mechanical properties of the surrounding extracellular and

29   pericellular matrix at a sub-cellular length scale. OptoRheo can be used in two operational

30   modalities (with and without an optical trap) to extend the dynamic range of microrheology

31   measurements. We corroborated this by characterising the ECM surrounding live breast

32   cancer cells in two distinct culture systems, cell clusters in 3D hydrogels and spheroids in

33   suspension culture. This cutting-edge instrument will transform the exploration of drug

34   transport through complex cell culture matrices and optimise the design of the next-

35   generation of disease models.

36

37   **Introduction**

38   Cells sense and respond to the mechanical properties of the extracellular matrix (ECM) at a

39   cellular length scale, using traction forces to probe stiffness [1], steer migration [2,3] and

40   influence cell fate [4]. Simultaneously, the ECM is continuously remodelled by cells as they

41   exert these traction forces [5] during cell migration and morphological re-arrangement [6].

42   Anomalies in the mechanical properties of the ECM play significant roles in the development

43   of pathologies such as cancer [7] and fibrosis [8], often establishing barriers to therapeutic

44   intervention [9]. Modelling and understanding cellular influence on ECM biomechanics is

45   challenging given the wide range of mechanical environments experienced in health and

46   disease. In healthy tissues, the elastic modulus has been reported to range from tens of Pa

47   (e.g., brain, lung) to well above 10 KPa (e.g., skeletal muscle, bone), with disease states

48   such as cancer and fibrosis showing a significant change in stiffness (e.g., from 800 Pa for

49   normal breast to more than 4 KPa in breast cancer) [10]. Moreover, the full mechanical

50   characterisation of the ECM also contains a viscous component that may influence cell

51   behaviour [11]. The recent development of engineered hydrogels with tuneable mechanical

52   properties [12,13] have made it possible to recreate elements of the ECM micro-architecture *in*

53   *vitro* and reveal the influence of ECM viscoelasticity on cell processes [14,15]. Despite these

54   advances and their importance, the mechanistic processes of cell-matrix interactions remain

55 poorly understood. For instance, do cells 'prime' their local environment prior to migrating or

56 do they exploit existing weaknesses in the ECM and migrate accordingly? These

57 unanswered questions call for minimally invasive optical approaches to monitor changes in

58 the microscopic mechanical properties of the ECM, *in situ* and in real time, local to

59 proliferating cells over many days.

60

61 To address this aim, OptoRheo combines three different microscopy techniques, light sheet

62 microscopy, multiplane microscopy and optical trapping into a single instrument. This

63 approach enables live fluorescence imaging deep in 3D cell cultures and microrheology

64 measurements of the ECM within the same region of interest, local to and far from the cells.

65 3D fluorescence imaging is achieved using a new version of reflected light sheet

66 fluorescence microscopy (LSFM) [16–19] built on a commercial inverted microscope body to

67 image hundreds of microns deep from the coverslip, within live 3D cell cultures and with sub-

68 cellular resolution. The sample is kept completely stationary during z-scanning, with no

69 perturbation or contamination risk from dipping lenses, both crucial for ensuring that

70 observation does not influence the mechanical or biological properties of the sample. This

71 novel configuration allows for delicate samples such as hydrogel scaffolds to be imaged

72 simply in off-the-shelf chambered coverslips. To extract the viscoelastic properties of the

73 ECM, OptoRheo tracks the thermally driven Brownian motion of micron-sized beads, acting

74 as rheological probes across a wide time-window. The inert bead probes can be embedded

75 in the hydrogel during encapsulation [6,20–22] or even internalised into cells [23] to probe intra-

76 cellular viscoelasticity. In suspension cultures, an optical trap can be used to hold the probe

77 in the field of view within the cells' microniche during the measurement extending the range

78 of materials the instrument can characterise [24]. Finally, OptoRheo incorporates optional

79 multiplane imaging that can be used to extend microrheology to 3D in a configuration similar

80 to the one developed for OptiMuM [25], to achieve a full 3D characterisation of the extracellular

81 microenvironment.

82

83   To highlight the capability of OptoRheo, we present data obtained from the analysis of two

84   systems seeded with human-derived MCF-7 and/or MDA-MB-231 breast cancer cells, either

85   (I) encapsulated as clusters in 3D hydrogels or (II) as spheroids maintained in suspension

86   culture. In the case of hydrogel scaffolds, matrix stiffness was measured using passive

87   particle tracking microrheology without the use of an optical trap or multiplane imaging,

88   whereas in the case of suspension cultures, the optical trap was implemented along with

89   multiplane imaging. Imaging and microrheology were performed sequentially at multiple

90   regions within the samples at depths of 150 µm - 400 µm from the coverslip. In the case of

91   the hydrogels, the samples were monitored over three days to reveal microscale variations

92   in the elastic properties of the ECM near to and away from cells. When studying spheroids in

93   suspension the optical trap was used to place and hold the probes in user-defined locations

94   and extract the relative viscosity of the media near the spheroids. Notably, in both the cases

95   our measurements were found to be sensitive to local spatio-temporal variations in the

96   biomechanical properties of the culture medium. As demonstrated in this study, our

97   multimodal and minimally invasive approach opens a wide range of future opportunities for

98   physiologically relevant, long-time course investigations and time-lapse videos of cell-ECM

99   interactions in fragile live cell culture samples. We anticipate that this approach will be

100   applied to increasingly complex and relevant *in vitro* models, providing an essential insight

101   into the previously opaque mechanistic control of cell behaviour by the ECM in health and

102   disease.

103

104   **Results**

105

106   3D imaging deep in live cell cultures

107

108   A schematic representation of OptoRheo can be seen in Figure 1. 3D light sheet

109   fluorescence microscopy (LSFM) is achieved by projecting a thin, planar excitation

4

110   beam limited to the detection plane of the microscope and collecting the emitted

111   fluorescence at a 90° angle to the illumination plane [26,27]. For deep imaging of live 3D cell

112   cultures, the light sheet illumination was introduced using a 10 mm 90:10 (Reflectance:

113   Transmittance) beam splitter cube placed in the sample chamber prior to casting the gel

114   alongside it (Figs 1, 2 and S1). This LSFM approach has multiple advantages; deep and fast

115   fluorescence imaging with low phototoxicity [28] and minimal sample perturbation during

116   imaging, while being cost-effective and modular. The glass beam splitter cube can be

117   sterilized for reuse and placed either inside or outside the sample chamber to provide

118   flexibility to adapt to different experimental conditions.

119

120   Unlike some other prism or mirror based LSFM solutions [16,29,30], 3D image generation was

121   achieved here by scanning the light sheet and not the sample. Notably, this allows the

122   sample to be kept stationary and undisturbed throughout data collection, which is essential

123   for imaging delicate samples prepared in soft hydrogels (Fig 2A) or liquid suspension media

124   over multiple days. The light sheet itself was generated using a cylindrical lens, the

125   properties of which set the thickness of the light sheet and influence the axial resolution and

126   optical sectioning capabilities of the microscope. In the presented configuration, the

127   measured axial resolution of the detection optics of the LSFM on OptoRheo was 1.09 μm for

128    $\lambda_{ex} \backslash \lambda_{em}$ = 532 nm \ 580 nm which agrees closely with theory (1.1 μm) (Fig S2).

129   A scanning galvanometer mirror was placed conjugate to the cylindrical lens using a 4f

130   system, so that tilting the galvanometer mirror translated to a Z-shift in position of the light

131   sheet at the sample (Fig 1). Acquiring Z-stacks involved synchronisation of the galvanometer

132   mirror with a piezoelectric objective scanner that moved the objective lens, ensuring that the

133   illumination and imaging planes remained co-aligned and synchronised throughout the scan.

134   The light sheet remained at optimal thickness (~3 μm for all three colour channels, see

135   Methods) over a field of view of ~100 μm. However, image tiling could be achieved within a

136   region 4 - 6 mm from the beam splitter cube to increase the field of view. This required

137   shifting the light sheet focus laterally by moving the position of the cylindrical lens. The

138   shifted position of the beam splitter was compensated by tilting the galvanometer mirror to

139   image the new focal position.

140

141
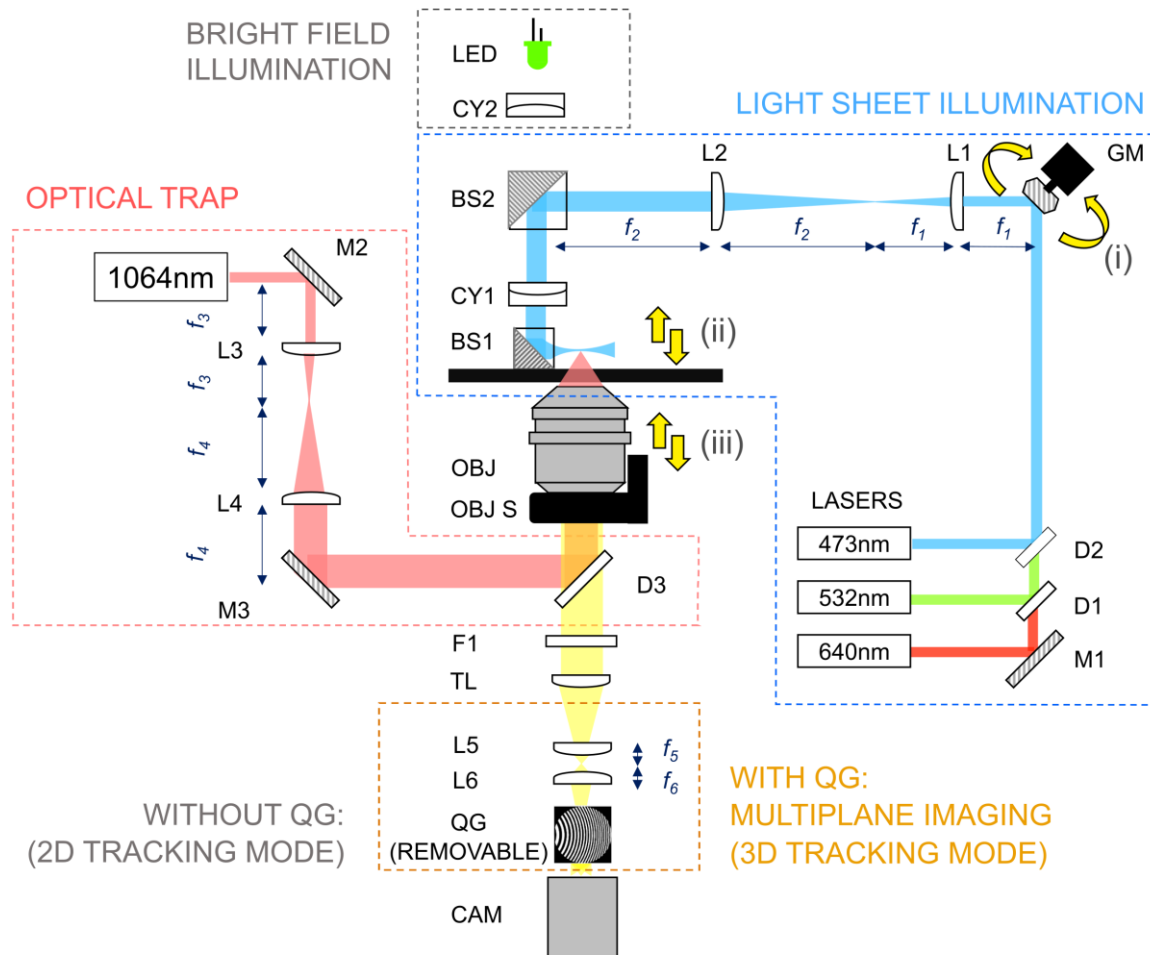
142

143   Figure 1: **A schematic representation of the OptoRheo instrument**. Components: Lasers

144   – 473 nm, 532 nm and 640 nm lasers provide the light sheet illumination while a 1064 nm

145   laser is used for optical trapping. M1- M3 – mirrors; D1-D3 – dichroic mirrors; L1-L6 –

146   achromatic doublets, L1 and L2 form a 8.3 x beam expander and are part of a 4f system with

147   the galvanometer mirror (GM) and a beam splitter (BS2); CY1, CY2 – cylindrical lenses;

148   BS1, BS2 – beam splitter cubes; OBJ – objective lens; OBJ S – piezoelectric objective

149   scanner; F1– fluorescence emission filter; TL – tube lens, QG – quadratic gratings and CAM

150   – camera. Yellow arrows indicate synchronised motion of (i) the galvanometer mirror, (ii) the

6

151   projected light sheet and (iii) the objective lens (using a piezoelectric objective scanner). The

152   quadratic gratings slide in and out of the optical path to enable 2D and 3D particle tracking.

153   The quadratic gratings are removed for the LSFM imaging.

154

155   The current configuration of OptoRheo uses a 60x objective lens with a 1.5 mm working

156   distance and a numerical aperture (NA) of 1.1, selected to image deep into a sample, but

157   with a high enough NA for optical trapping. For the data presented in this work, z-scans were

158   typically recorded 150 µm - 400 µm from the coverslip (Fig 2B). To extend the field of view

159   for larger objects, LSFM images could be tiled and stitched together as detailed above. The

160   multiplane grating breaks up the field of view into nine planes to enable 3D tracking of the

161   rheological probe [25] and therefore, is not required for LSFM imaging and can be easily

162   removed by means of a slider. Additionally, the multiplane gratings used were optimised for

163   a particular wavelength (543 nm) making them unsuitable for multicolour imaging. OptoRheo

164   is fitted with a stage-top incubator that regulates temperature, CO_2 and humidity around the

165   sample, allowing long time-course experiments spanning over hours (Fig 2C and

166   Supplementary Videos VS1 and VS2) and days.

167
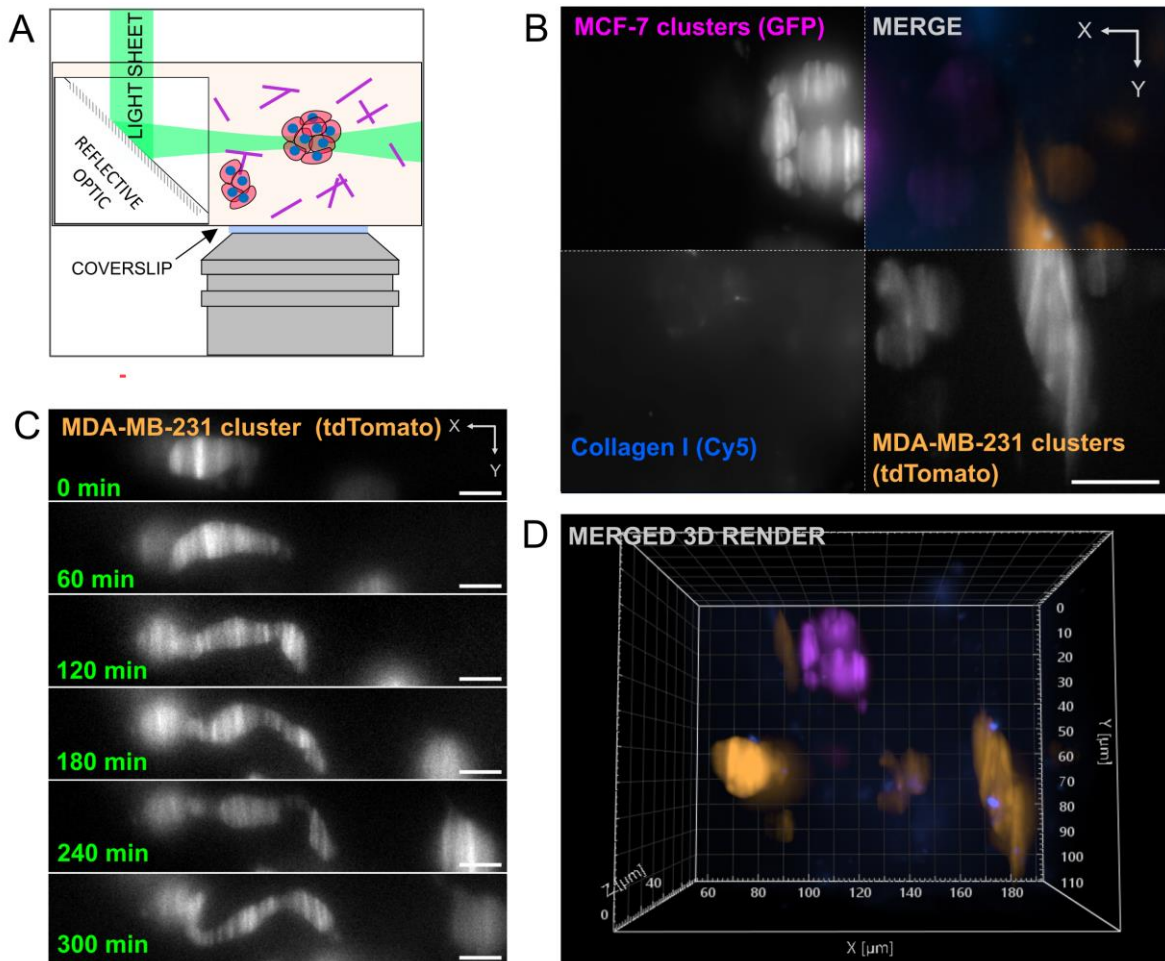
168
169 Figure 2: **Light sheet fluorescence microscopy (LSFM) with OptoRheo.** A. Schematic of

170 light sheet microscopy on the OptoRheo. Sample consists of cell clusters (represented by

171 red circles with blue centres) and collagen (purple lines). B. Multicolour imaging of a co-

172 culture of MCF-7 (top left corner of montage) and MDA-MB-231 (bottom right corner) in

173 hydrogel supplemented with Cy-5 labelled collagen I (bottom right corner) on the OptoRheo

174 with three colour channels. Images in montage are maximum intensity projections. Scale bar

175 = 20 µm. C. Single planes from time lapse movie (supplementary video VS1) taken on the

176 OptoRheo of a MDA-MB-231 cell changing morphology. Scale bar = 10 µm. D. 3D rendering

177 of the same region of interest in panel B.

178

179

180 Microrheology of gels and suspension cultures

8

181

182   The viscoelastic properties of biomaterials can be extracted non-invasively using particle

183   tracking microrheology as developed by this group and others [24,25,31]. This involves a

184   statistical analysis of the residual Brownian motion of micron-sized spherical probes, whose

185   temporal behaviour can be described by means of a Generalised Langevin equation [31]. For

186   this purpose, polystyrene microsphere probes were seeded in the cell culture samples under

187   sterile conditions (Fig 3A). For hydrogel-based cell culture systems, the diameter of the

188   microsphere probes (6 μm) was selected so that the Brownian motion of the probes were

189   constrained by the hydrogel polymer network. A small field of view (typically 14 μm x 14 μm)

190   was recorded around the microsphere probe (Fig 3B) to track the trajectory of each probe

191   (Fig 3C) at a relatively high frame rate (~ 300 Hz - 5 kHz) to achieve broadband

192   microrheology. This was done while switching the illumination to transmission mode using a

193   LED source to avoid introducing fluorescence bleaching-related errors in particle tracking

194   (Fig 1). A second cylindrical lens (CY2 in Fig 1) was placed in the LED light path to

195   compensate for the presence of the light sheet forming cylindrical lens (CY1 in Fig 1) and

196   produce uniform illumination. An analysis of the mean squared displacement (MSD) of the

197   confined microspheres (Fig 3D) gives the elastic ($G'(\omega)$) and viscous ($G''(\omega)$) moduli of the

198   surrounding gel (Fig 3E), see methods section for further details.

199

200

201
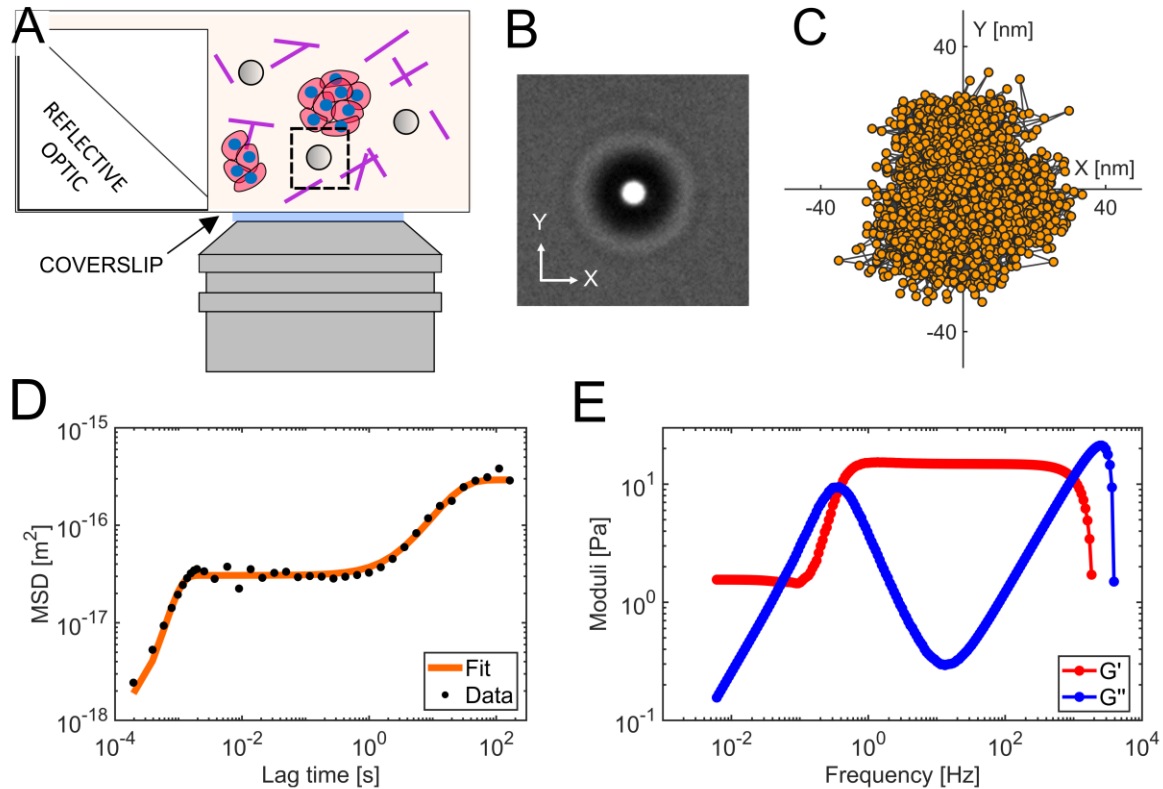
Figure 3: **Passive microrheology without optical trapping.** A. A schematic representation of passive microrheology measurements. B. Microsphere probes (6 μm diameter) were seeded in the hydrogel and small regions of interest (typically 14 μm x 14 μm as shown) around them were imaged at a high frame rate (5 kHz in this example). C. Particle trajectory in a 2D plane with individual positions depicted in orange (down sampled here for clarity from a total of 1.5×10^6 frames). D-E. The mean squared displacement (MSD) provides a measure of gel compliance, which is then used to compute the elastic ($G'(\omega)$) and viscous ($G''(\omega)$) moduli of the gel over a wide range of frequencies as shown in panel E (for more details on the analysis see Methods).

In liquid media and suspension cultures, microsphere probes sediment to the coverslip over time with a rate dependent on the gravitational force, the buoyancy of the microsphere and the viscosity of the medium [32]. In aqueous liquids, this sedimentation rate is about 20 μm/s for microspheres with a 3 μm radius, thus preventing long-term (i.e. tens of minutes) tracking of the probe trajectories, which are needed for broadband microrheology calculations.

10

217 Therefore, when working with liquids we used an optical trap (Fig 4A) to hold the probe in

218 the field of view and at the required location relative to the cell/s of interest during the

219 measurement time. The trapping force acting on the microsphere was kept very low (<10^{-6}

220 N/ m) by controlling the laser power, to maximise the amplitude of the residual Brownian

221 motion, increasing the sensitivity of the microrheology measurement and the frequency

222 range. The confined Brownian motion of the microsphere could then be recorded at ~300 Hz

223 in 3D by inserting a removable pair of quadratic gratings (QG) in the detection path before

224 the sCMOS camera to achieve multiplane detection of the particle position [25,33] (Fig 1 and

225 4B). In particular, the quadratic grating pair focus light from nine object-planes as an array

226 onto the camera sensor for instantaneous 3D imaging without the need of any mechanical

227 moving parts [25,33] (Fig 4B). This method allows tracking of the microsphere motion in all

228 three dimensions simultaneously (Fig 4C), revealing spatial variation of the sample's

229 viscoelastic properties. However, the smallest variance in particle position we could reliably

230 measure with the present configuration was 30 nm in z, compared to 15 nm in x and y.

231 Therefore, tracking in z was unreliable for our gel samples where the motion is typically less

232 than 50 nm (see Fig 3C).

233

234 We validated our microrheology measurements from the 3D particle tracking mode of

235 OptoRheo by using water, a well characterised Newtonian fluid. We extended our previous

236 work [25] by measuring the 3D trajectories of microsphere probes from 50 to 400 μm away

237 from the coverslip, without the use of any aberration correction, thus enabling microrheology

238 measurements at the same sample depths as our light-sheet imaging experiments. It is

239 important to note that most studies employing optical trapping report measurements taken at

240 <100 μm from the coverslip [34]. The use of water immersion and a correction collar allowed

241 us to achieve trap stiffness k values of k_x= 3.2 x 10^{-7} ± 0.3 x 10^{-7} N/m along the x axis, k_y =

242 3.2 x 10^{-7} ± 0.5 x 10^{-7} N/m along the y axis and k_z = 6.7 x 10^{-8} ± 1.2 x 10^{-8} N/m along the z

243 axis (mean ± standard deviation) over this large range of distances from the coverslip.

244   Relative viscosity (ratio of viscosity of an aqueous solution to the viscosity of water at the

245   same temperature) could be evaluated in 3D by analysing the normalised position

246   autocorrelation function (NPAF) for x, y and z at depths ranging from 50 µm to 400 µm from

247   the coverslip. In particular, the relative viscosity can be read "*at a glance*" from the abscissa

248   of the NPAF intercept e^{-1}, when the NPAF is plotted versus a dimensionless lag-time $\tau^* =$

249    $k\tau/(6\pi a\eta_s)$; where k is the trap stiffness, τ is the lag-time (or time interval), a is the probe

250   radius, and η_s is the Newtonian viscosity expected for the pure solvent [35] (Fig 4D). Figure 4E

251   shows the mean x, y and z relative viscosity ± standard deviation, performed at different

252   depths (see Methods). Over the range of recorded measurements, the measured mean

253   relative viscosity (over x, y and z) remained stable with depth (i.e., 1 ± 0.05).

254

255
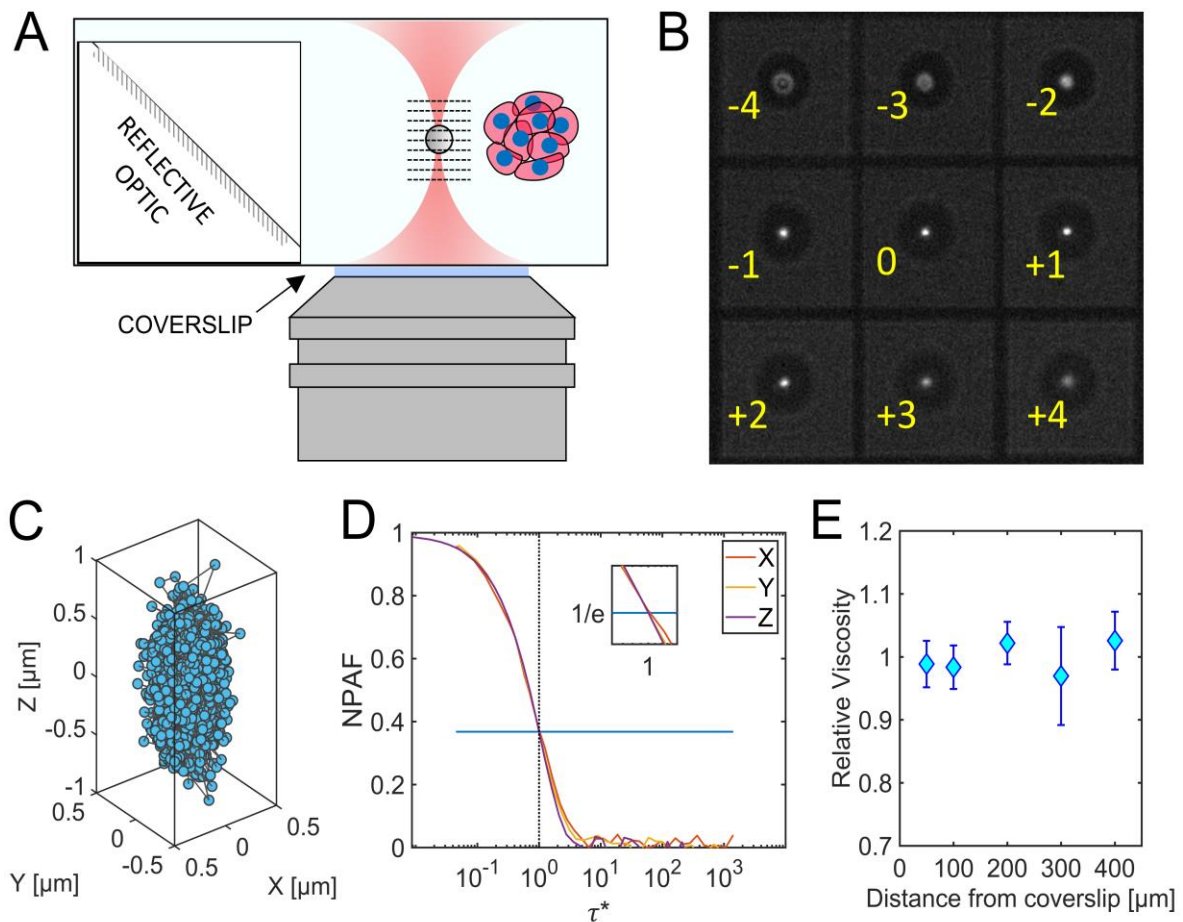
256
257   Figure 4: **Microrheology with an optical trap and multiplane detection** (3D particle

258   tracking mode) in an aqueous solution. A. An optically trapped microsphere is imaged in 9

259   planes simultaneously (planes represented by dashed lines). B. Captured image of nine

260   separate Z planes (Δz = 0.79 μm). The planes (labelled from number -4 to +4) are

261   simultaneously recorded at the camera sensor to extract the 3D trajectory. C. The resulting

262   3D trajectory of optically trapped microsphere in water with individual positions depicted as

263   blue circles (down sampled for clarity from a total of 2 x 10^5 frames). D. The normalised

264   position autocorrelation function (NPAF) versus a dimensionless time, τ^*. E. The mean ±

265   standard deviation of the relative viscosity measured at each position over a range of

266   depths.

267

268   Monitoring ECM stiffness in hydrogel-encapsulated 3D cell culture

269

270   In order to test the ability of OptoRheo to evaluate biomechanical properties of the ECM in

271   real time, clusters of human-derived MCF-7 cancer cells expressing the tdTomato

272   fluorescent protein were grown in a hydrogel-encapsulated cell culture matrix [12,36]. Echoing

273   what is known from patients, changes in the ECM stiffness around these cells have been

274   correlated with cancer progression and metastasis, and have been shown to alter drug

275   resistance [37,38]. Complementary multi-colour 3D LSFM imaging allowed cells and labelled

276   matrix components (i.e. collagen I) from the same locations to be captured in separate

277   colour channels. These volume images could be overlaid and combined with microrheology

278   measurements to map the changing biomechanical properties to the changing morphology

279   of the sample, at the microscale. This approach was used to compare four different complex

280   systems made of hydrogels with and without (i) collagen and (ii) cells.

281

282   The curves of the elastic ($G'(\omega)$) and the viscous ($G''(\omega)$) moduli of all the hydrogel

283   preparations show a pattern characteristic of viscoelastic polymer gels [39] with a rubbery

284   elastic plateau G'_0 (where $G'(\omega) > G''(\omega)$) at low frequencies transitioning to a high

13

285   frequency glassy state (Figs 3E and 5A). Environmental control on OptoRheo allowed the

286   gel samples to be kept under physiological conditions over multiple days, making it possible

287   to re-visit selected microsphere probes multiple times over the duration of the experiment

288   (three days) to follow the changing ECM properties over time. This was performed in

289   triplicate.

290

291   In the absence of cells, the height of the elastic plateau - G_0', is greater for plain gels (n = 11)

292   as compared to gels supplemented with collagen I (n = 11) (p = 0.0014, Kruskal-Wallis test;

293   Fig 5A) at the start of the experiments (day 1), indicating stiffer gels and may point to

294   differences in the cross-linked network [40]. The high frequency glassy response which can be

295   attributed to local monomer relaxation [41] is similar for the gels (Fig 5A) which have the same

296   polymer hydrogel base at the same concentration. We therefore focus our analysis on the

297   G_0' values.

298

299   The presence of cells brings about complex changes in the gels which become more

300   apparent over time and when taking into account the proximity to cell clusters (Fig 5 B-F).

301   Over time, as cell clusters proliferated and changed their relative distance from the probes,

302   this information could be extracted from LSFM images. Our data show that the presence of

303   collagen makes the gels more compliant (p = 0.0008 Generalised Mixed Effects Model).

304   There was a significant difference in the proportional change in $\Delta G_0'$ (between day 3 and day

305   1) in the presence and absence of cells in gels supplemented with collagen (p = 0.007,

306   Kruskal-Wallis test; Fig 5B). Moreover, the G_0' values change with distance from the nearest

307   cell cluster both in the presence and absence of collagen. In the presence of collagen, the

308   gel was most compliant within 50 µm from the edge of the nearest cell cluster. This region

309   near the cell clusters was much more heterogeneous with measurements spanning over

310   three orders of magnitude as compared to farther away (two orders of magnitude at regions

311   > 50 µm) (Fig 5F) hinting at a gel remodelling front.

14

312

313

314
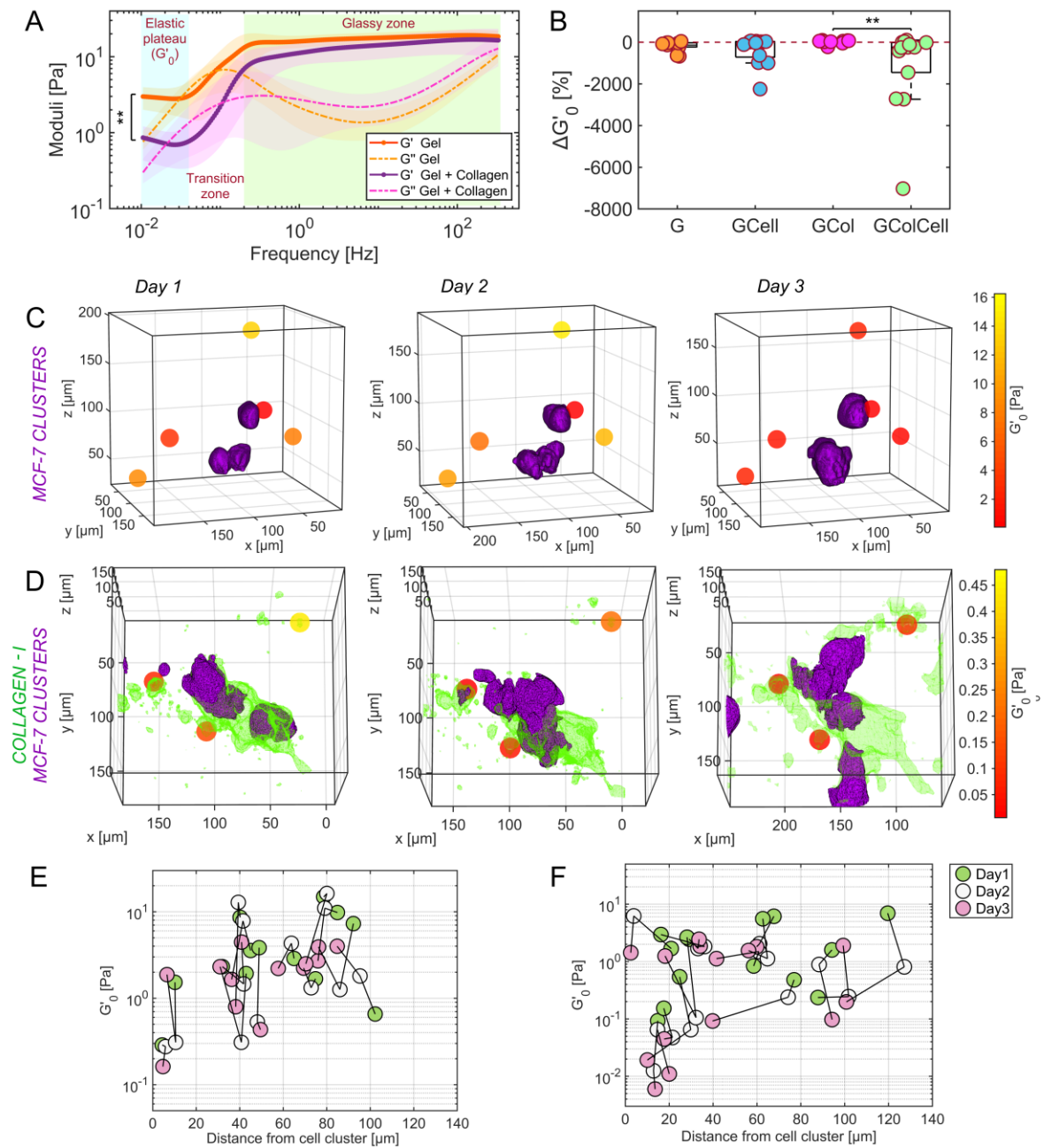
Figure 5: **Local stiffness measured in live 3D cell cultures with different compositions**.

A. Complex moduli of plain gel in orange and gel supplemented with collagen in purple at day 1 (averaged with 95% confidence intervals shown as shaded regions). B. Proportional change in the height of the low frequency elastic plateau G'_0 at individual bead probes over three days of observation in plain gel (G), gel with collagen (GCol), gel seeded with cells

15

320   (GCell) and gel with collagen and cells (GColCell). The dashed line represents no change,

321   negative values indicate more compliant gels. C-D. Biomechanical maps produced by

322   OptoRheo of MCF-7 clusters expressing tdTomato (shown in purple) encapsulated in

323   hydrogels and D. MCF-7 clusters from the same cell line in hydrogel supplemented with

324   collagen I labelled with Cy5 (shown in green) monitored over three days. Spheres depict

325   microsphere probes (not to scale) assigned a colour to reflect the local stiffness (G_0'). E. & F.

326   Spatiotemporal changes in G_0' values with relative distance from the edge of the cell clusters

327   in gel in the absence (E) and presence (F) of collagen over three days.

328

329   Mapping relative viscosity local to spheroids in suspension culture

330

331   The second scenario tested as a proof-of-concept, was to acquire 3D images and

332   microrheology measurements near spheroids in suspension culture. Spheroids were grown

333   from the same MCF-7 cancer cell line as in the peptide hydrogel cultures and were used two

334   days after seeding at a size of ~1 mm in diameter. As both 3D imaging and microrheology

335   on OptoRheo do not involve moving the sample, these spheroids could be maintained in

336   liquid media without the need to immobilise them in agarose or any other hydrogel matrix –

337   an advantage over most conventional LSFM instruments. Volume images near the edges of

338   spheroids were acquired by tiling multiple overlapping imaging volumes of 200 μm x 200 μm

339   x 200 μm (between 150 μm – 350 μm from the coverslip) (Fig 6A). Once the images were

340   acquired, the instrument was switched from LSFM modality to 3D particle tracking mode by

341   sliding the quadratic gratings into the optical path and with illumination in transmission (QG

342   in Fig 1). The optical trap enabled microsphere probes to be individually trapped and

343   positioned in 3D with the XY stage and the piezoelectric objective scanner to make

344   measurements at selected locations near the edge of the spheroids (Fig 6A inset).

345

346   Our measurements show an apparent increase in relative viscosity with decreasing distance

347   (4 μm, n = 4; 6 μm, n = 4; 12 μm, n = 3 and 30 μm, n = 7) between the centre of the

348   microsphere and the surface of the spheroid (n = 2 spheroids) (Fig 6A, 6B and 6C).

349   Viscosities could be extracted in 3D by resampling the recorded 3D trajectories along any

350   desired axis, calculating the MSD, and then using Fick's Law (see methods). Such angle-by-

351   angle analysis reveals higher relative viscosity values perpendicular to the surface of the

352   spheroid as compared to parallel to the surface, with the anisotropy increasing as the probe

353   approaches the surface (Fig 6B). This trend is in agreement with predictions from Faxén's

354   law which describes the increased hydrodynamic drag experienced by objects near solid

355   surfaces and manifests itself as an increase in apparent viscosity, albeit our measured

356   values are lower than the predictions [42] (dashed black line in Fig 6C). The lower values could

357   potentially be attributed to the spheroid surface being irregular and not completely inelastic.

358   Additionally, the presence of salts in the nutrient medium may screen charge-charge

359   interactions between the microsphere probes and the cell surface, reducing the force

360   required to move the probe closer to the spheroid surface [43] as corroborated by control

361   measurements at corresponding distances from the inert glass coverslip in the same

362   medium without the presence of the spheroids (red line in Fig 6C).

363

364
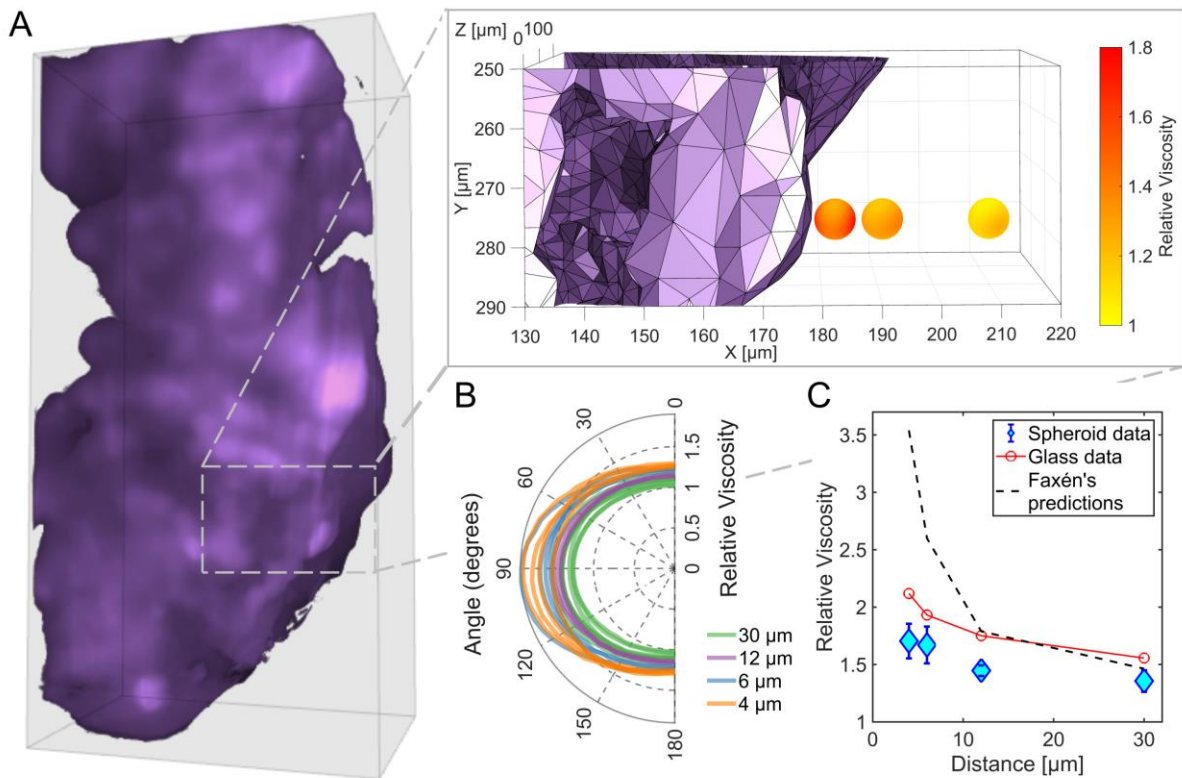
Figure 6: **Viscosity near spheroid**. A. 3D rendering of a section of a spheroid of MCF-7 cells expressing td-Tomato (relative dimensions: 200 µm x 400 µm x 100 µm (150-250 µm from the coverslip)). The inset shows one of the areas where viscosity (relative to the solvent) measurements were acquired at incremental distances from the spheroid surface – three measurements (4 µm, 12 µm and 30 µm from the spheroid surface) are depicted as spheres (not to scale). The colour gradient for each sphere represents the relative viscosity sampled by angle at each measurement position. A fourth position (6 µm) has not been shown to aid visualisation. B. Relative viscosity measurements in a plane perpendicular to the spheroid surface, passing through the highest and lowest measured viscosity at the probe position. C. Mean ± standard deviation of relative viscosity measurements of the nutrient media at each position for a direction perpendicular to the spheroid surface (blue) and glass (red), showing increased apparent viscosity at positions closer to the surface but lower than values predicted from Faxén's law (black dashed line).

Discussion

380

381   To understand how cells interact with and remodel their surrounding matrix, it is crucial not

382   only to visualise cell clusters in 3D, but also to map these images to the changing micro-

383   mechanical properties of the matrix local to and distant from the cells. In this study, we have

384   introduced an integrated instrument – OptoRheo, that combines light sheet fluorescence

385   microscopy (LSFM) with non-invasive microrheology to enable a more complete

386   understanding of cell-matrix interactions. The new LSFM configuration presented here is

387   straightforward to implement and does not require the use of bespoke, expensive optics.

388   This reflected configuration allows for samples to be prepared and mounted as on any

389   commercial inverted microscope, using off-the-self sample chambers and a stage-top

390   incubator to control temperature, humidity and CO_2 throughout experiments, enabling

391   delicate hydrogel-based cell culture samples to be studied over multiple days. With the

392   ability to optically trap microrheological probes when required, we have demonstrated the

393   capability of the instrument to study aqueous (suspension culture) as well as soft solid

394   (hydrogel) environments. This modular functionality with a gratings-based approach allows

395   OptoRheo to transition from 2D to 3D particle tracking without difficulty. We provide

396   experimental evidence of this approach by following changes in matrix viscoelasticity in 2D

397   in hydrogel-encapsulated cell cultures over three days and viscosity in 3D near spheroids in

398   suspension. Our localised rheological measurements reveal heterogeneities at the

399   microscale in hydrogel-encapsulated cell cultures.

400

401   OptoRheo provides broadband microrheology measurements, covering 5 - 6 decades of

402   frequency in our data. These broadband measurements provide valuable insight into the

403   frequency-dependent mechanical properties of biological materials. As can be seen in Figure

404   5, OptoRheo is sensitive to mechanical changes arising from changes in matrix composition

405   and from cell-driven re-organisation of the local environment, detectable over a broad range

406   of frequencies. This is in contrast to Brillouin scattering – another emerging technique that is

19

407   being used to quantify the mechanical properties of biological systems [44], but which is limited

408   to a narrow range of frequencies in the gigahertz regime. It is possible that the narrow

409   frequency range of Brillouin scattering measurements will miss some of the mechanical

410   changes we report here. Furthermore, compared to previously published methods for optical

411   trapping based stiffness measurements [45,46], OptoRheo can characterise samples at depths

412   of hundreds of microns from the coverslip making it particularly suited to cell cultures grown

413   in 3D. OptoRheo has the additional benefit that the mechanical characterisation is paired

414   with multi-channel 3D fluorescence light sheet imaging allowing the changing morphology of

415   the cells to be monitored at the same time.

416

417   Extending the rheological measurements to 3D and sampling viscosity in 360 °, as shown in

418   our experiments with spheroids in suspension (Fig 6B), increases the capability of our

419   measurements to extract heterogeneities, not just between probe positions, but for different

420   directions at a single probe position. Currently, this 3D approach is restricted to computing

421   viscosity in liquids due to limited spatial sensitivity when tracking probe position in z

422   (Methods). This is not an issue when the extent of the Brownian motion of the probe is large,

423   such as the ~1 μm (Fig 4B) observed in a weak optical trap in suspension culture, but is of

424   concern when motion is very small (≤ 50 nm) such as that observed in stiff gels (Fig 3B). In

425   future, the sensitivity and measurement range of the 'sharpness' metric used for particle

426   tracking in z could be tuned by changing the plane spacing selected with the multiplane

427   grating pair, the probe size, the illumination levels and the signal to noise ratio of the images

428   [25]. Efforts to extend these 3D analyses to gels in the future would be highly valuable as

429   biophysical properties in the ECM are likely to vary in 3D, as apparent in the images of

430   labelled collagen present in the gel samples (Fig 5B).

431

432   The outputs from these proof-of-concept experiments are very data-rich. Different locations

433   of interest in the sample can be programmed to be revisited multiple times over a multi-day

434   experiment. As such, OptoRheo enables researchers to track numerous variables over time,

435   so that the relative cell and probe position, and cell behaviour (change in shape or size,

436   migration, apoptosis) can be related to viscous and elastic components of the matrix

437   biophysical properties. In future, it would be relatively straight forward to include additional

438   probes into the sample (either genetically engineered reporters in the cells or sensors

439   embedded in the gel/ matrix) to track the coordinated impact of chemical, biological and

440   mechanical cues.

441

442   As highlighted in recent publications [4,47], the control of cell behaviour by mechanical forces

443   exerted through the ECM remains poorly understood, even as researchers take advantage

444   of ECM control to create more complex, physiologically relevant models of development and

445   disease, that better represent the *in vivo* micro-environment. The ability to integrate read-

446   outs of cell behaviour with the microrheology of pericellular and distant matrix will be critical

447   in further improving these models and using them to uncover the mechanistic basis of the

448   phenomena they imitate. In addition, for development of therapeutics, there remains a

449   significant gap in our understanding of the environments that drugs and delivery vehicles

450   encounter in the body. The simultaneous observation of material transport together with

451   rheological measurements will enable us to build detailed structure-function relations of drug

452   delivery pathways, which in turn, will enable more efficient screening of candidate

453   therapeutics and better predictive models of *in vivo* activity and efficacy.

454

455

456   **Online Methods**

457

458   Light sheet fluorescence microscopy (LSFM)

459   OptoRheo uses a reflected light sheet configuration where light sheet illumination is

460   introduced into the imaging plane of an inverted microscope (Olympus IX-73) using a right-

461   angle optic (90:10 RT beam splitter cube, 10 mm; Thorlabs Inc.). Z-scanning was achieved

21

462   by moving the light sheet through the sample using a galvanometer scanning mirror

463   (dynAXIS 3S; SCANLAB Gmbh) whilst simultaneously moving the

464   objective lens (LUMFLN60XW 60x 1.1 NA 1.5 mm WD; Olympus) via a

465   motorised piezo objective scanner (P-725.4CD; Physik Instrumente Ltd.) to keep the light

466   sheet in focus. Lateral positioning was achieved using a XY microscope stage (MS-2000,

467   ASI) and a zoom-mount attached to the cylindrical lens forming the light sheet. The

468   fluorescence image was detected using an sCMOS camera (Hamamatsu ORCA Flash 4.0

469   V2). Environmental control was achieved using an Okolab stage-top incubator (H301-K-

470   FRAME) supplied with pre-mixed CO_2 gas.

471

472   Multi-colour fluorescence imaging was made possible by using three lasers separately to

473   form the light sheet; 473 nm (SLIM-473; Oxxius), 532 nm (BWN-532-2OE; B&W Tek) and

474   640 nm (OBIS; Coherent). These laser lines were coupled to each other in the illumination

475   beam path using dichroic mirrors. A cylindrical lens (f = 50 mm, Thorlabs) was used to

476   generate the light sheet with a beam waist of 2.6 μm for λ_{ex} 473 nm, 2.4 μm for λ_{ex} 532 nm

477   and 3.3 μm for λ_{ex} 640 nm. The light sheet was aligned and characterised by imaging it in

478   reflection using two beam splitters (90:10 RT beam splitter cube, 5 mm; Thorlabs Inc.) in

479   tandem. The relationship between voltage applied to the galvanometer mirror and position of

480   the light sheet was characterised using this double beam splitter set up and keeping the

481   detection objective stationary while scanning the light sheet in z. The slope of the linear fit to

482   the measured position of the light sheet against the voltage applied gave the pixel to voltage

483   step size for synchronised movement.

484

485   When imaging samples, an autofocus step is first performed to ensure the illumination and

486   detection optics, primarily the objective, are aligned. This involves recording a stack of

487   images while keeping the imaging objective stationary and scanning the light sheet with a

488   sub-beam-waist step size. The frame with the highest mean intensity value denotes where

489   the light sheet waist coincides with the imaging plane and so the position of the light sheet

490   for this frame is synchronised with the height of the objective.

491

492   Standard off-the-shelf beam splitter cubes have a blunt edge that make the bottom 150 µm

493   unsuitable for reflecting the light sheet illumination. These regions can be illuminated by

494   tilting the light sheet at BS1 (Fig 1) or by using a bespoke cube with a sharp edge.

495

496   The mechanical components of the OptoRheo including the light sheet parts were controlled

497   in LabVIEW (2018, 64bit; National Instruments Inc.). Image volumes were saved as '.tiff'

498   files. Automation of the laser lines through camera-controlled remote triggering and a

499   motorised filter turret enabled overnight time lapse imaging.

500

501   Image processing

502   Contrast adjustment and background subtraction was performed on image volumes in

503   ImageJ/ Fiji [48] and volume tile stitching was performed using the BigStitcher [49] plugin for Fiji.

504   3D rendering for Figure 6A was done in FluoRender (v 2.26.3) [50] and for Figure 2B was done

505   in Imaris (10.0.0, Oxford Instruments).

506

507   To calculate the distance between microspheres and the nearest cell clusters, the centre

508   positions of the microspheres in image coordinate space were extracted from the LSFM

509   images. Although the microspheres (Polybead® Microspheres 6.00 µm; PolySciences) were

510   not fluorescently labelled, they are identifiable in the 3D LSFM images due to light scattering.

511   Mesh renderings of the corresponding cell clusters were exported from FluoRender and

512   these meshes along with positions of the microspheres from the same image volume were

513   used as inputs in the point2trimesh.m [51] code in MATLAB which computes the shortest

514   distance between a given point and the outer edge of a triangular mesh.

515

23

516   Figures 5C and 5D and the inset within 6A were prepared in MATLAB using mesh

517   renderings generated in FluoRender overlaid with rendered spheres to depict the

518   microsphere probes with a colour gradient to show the low frequency plateau in the elastic

519   modulus (G'_0) (Fig 5C and 5D) or viscosity (Fig 6A inset) at each probe.

520

521   Optical Tweezers

522   The beam path from a continuous wave 1064 nm 5 W DPSS laser (Opus, Laser Quantum)

523   was directed into the inverted microscope body and focused in the image plane using the

524   same objective lens used for imaging in the LSFM set up. This objective lens was also used

525   to image a small region of interest (14 μm x 14 μm), required for high frame rate imaging,

526   around the trapped polystyrene microspheres in wide-field with illumination in transmission

527   for fast (300 Hz for multiplane 3D rheology) tracking of thermal fluctuations.

528

529   Multiplane detection

530   3D imaging of the microrheology probes was made possible by multiplane detection similar

531   to the OpTIMuM instrument [25] and its predecessors [33,52]. Here, a multiplane grating pair was

532   formed using two quadratically distorted diffraction gratings etched into a quartz substrate

533   (bespoke production by Photronics UK Ltd). A single grating generates three sub-images,

534   corresponding to the m = 0, ± 1 diffraction orders while two gratings with orthogonal etch

535   patterns, can generate nine different sub-images, each corresponding to a different image

536   depth which can be captured simultaneously on a single camera sensor (Hamamatsu ORCA

537   Flash 4.0 V2) (Fig 4A). A 4f image relay system consisting of two 300 mm lenses was set up

538   in the detection path between the camera and the inverted microscope body to enable the

539   multiplane grating pair to be placed in the telecentric position. This set up ensured a

540   consistent level of magnification in each of the imaging focal planes. The grating is on a

541   slider and easily removable allowing the user to switch between standard full field of view

542 imaging and multiplane imaging of a small region of interest with no adverse side effects. In

543 our system we have used a relay and grating combination that gives plane separation of Δz

544 = 0.79 μm with the nine images spanning 7.11 μm, designed to show the extent and position

545 of our 6 μm diameter probe. Grating combinations can be chosen to suit the diameter of the

546 probe such that the total span in z covers the extent of the trajectory of the probe with the

547 minimum plane separation for optimal resolution [25].

548

549 Microrheology

550 Particle tracking microrheology was performed using polystyrene microspheres as probes

551 (Polybead® Microspheres 6.00 μm diameter; PolySciences). In hydrogel cultures, the

552 microspheres were encapsulated during the gelation process at a final density of 3×10^5

553 particles/ mL. In suspension cultures, the microspheres were added to a final dilution of

554 1:200,000 from concentrate product, the probes were individually optically trapped using ~4

555 mW of laser power (at the sample) and moved to a position of interest. The Brownian motion

556 of the microspheres, was recorded over 300,000 frames at ~300 frames per second for

557 experiments in Figures 4 and 5, and for 1.5×10^6 frames at 5 kHz for Figure 3 and the

558 measurements depicted in the time lapse videos (VS1 and VS2) using OptoRheo with

559 illumination in transmission from an LED light source (Fig 1). Videos of the microsphere

560 probes were acquired using Micro-Manager (version 1.4) [53] and Micro-Manager (version 2.0)

561 for Figure 3 and the measurements corresponding to the time lapse videos.

562

563 The time-dependent trajectories of the microspheres were extracted from these videos in

564 MATLAB (2019b; MathWorks, Nattick, MA). For 2D trajectories along the image plane a

565 centre-of-mass detection method following Otsu's method of multiple thresholding (with two

566 levels) was used. Out-of-plane Z motion of the probe was tracked by computing a

567 'Sharpness' metric as detailed in our OpTIMuM publication [25]. Particle tracking with these

568 methods gives us a minimum sensitivity of ~ 15 nm (FWHM) in the xy plane and ~ 30 nm

569   (FWHM) in z for a particle with diameter of ~ 6 μm, using a 60x objective and a plane

570   spacing of ~ Δz = 0.79 μm [25]. A calibration step is performed for each microsphere before

571   taking a measurement by translating a lens (L4 in Fig 1) in the beam expander in the optical

572   path as described previously [25].

573

574   In the case of hydrogels, the Brownian motion of the microsphere confined within the gel

575   was recorded in 2D without the use of the optical trap or multiplane imaging. For these data,

576   an analysis of the mean squared displacement (MSD) gave the storage (elastic) and loss

577   (viscous) moduli of the gel. To acquire the viscoelastic measurements for each probe, first

578   each experimentally acquired trajectory was detrended to remove long-term drift and a

579   filtering step was performed to remove instrument noise. For the noise filtering, a Fourier

580   transform of each trajectory was used to identify sharp noise peaks characterised by a single

581   frequency width and using an amplitude threshold of 2×10^{-10} m. These noisy peaks,

582   attributed to electrical noise from the laboratory, were then removed from the data using a

583   custom multiband filter in MATLAB. The MSD values for each filtered trajectory was then fit

584   with a stretched bi-exponential of the form

$$MSD(t) = \left(A_1 \, exp\left(-\left(\frac{t}{\tau_1} \right)^{B_1} \right) \right) + \left(A_2 \, exp\left(-\left(\frac{t}{\tau_2} \right)^{B_2} \right) \right) \qquad (1)$$

586   A_1, A_2, B_1, B_2, τ_1 and τ_2 are fitting parameters. This approach mitigates any error generated

587   by the inherently finite nature of the measurements that affects the accuracy to which the

588   MSD is calculated especially at short-time scales (Fig 3). The MSD relates to the gel's time

589   dependent compliance J(t) [54] as follows,

$$MSD(t) = \frac{k_B T}{\pi a} J(t) \qquad (2)$$

591   where k_B is the Boltzmann's constant, T is the absolute temperature, and a is the radius of

592   the microsphere. The materials' complex shear modulus can be computed from the

593   materials' compliance by means of its Fourier transform $(\hat{J}(\omega))$

26

594
$$G^*(\omega) = \frac{1}{i\omega\hat{J}(\omega)} \ . \tag{3}$$

595 We used a new MATLAB based graphical user interface named π-Rheo (see code

596 availability statement) for evaluating Equations 2 & 3, to compute the Fourier transform of

597 the particles' MSD and the materials' complex modulus for passive microrheology

598 measurements. π-Rheo is underpinned by the algorithm introduced in i-RheoFT [55]. The real

599 and imaginary parts of the complex modulus give the elastic ($G'(\omega)$) and viscous ($G''(\omega)$)

600 moduli of the gel.

601

602 The elastic plateau of the gels G_0' (equivalent to $G'(\omega)$ at low frequencies) can be calculated

603 simply from the particles' time-independent variance $\langle r^2 \rangle$ using the formula:

604
$$G_0' = \frac{k_B T}{\pi a \langle r^2 \rangle} \tag{4}$$

605 For aqueous solutions, where 3D positions of the probe are tracked, the viscosity may be

606 extracted by fitting an exponential decay against the normalised position autocorrelation

607 function [35]. This method is highly effective for data aligned with the principal axes of the

608 optical trap (see Fig 4D). However, when calculating viscosity along vectors not aligned with

609 these axes using this method, the significant trap anisotropy along the z-axis introduces

610 artefacts as outlined in detail previously [56]. Alternatively, if the material under investigation is

611 purely viscous, then at very early times the MSD of the bead should behave as if the bead is

612 not trapped. Under these conditions, Fick's Law for unconstrained diffusion can be used to

613 extract viscosity in any arbitrary direction rather than just x, y, z at these early times. Fick's

614 law for motion in 1D is given by,

615
$$MSD_{(t,\theta,\varphi)} = 2D_{(\theta,\varphi)}t \tag{5}$$

616 where θ and ψ define the direction being probed and D is the diffusion coefficient for a

617 sphere of radius a in a liquid with viscosity η. From the Stokes-Einstein relation

618
$$D = \frac{k_B T}{6\pi\eta_{(\theta,\varphi)}a} \ . \tag{6}$$

619 This approach was used to compute viscosity in 3D as shown in Figure 4E and Figure 6A.

27

620

Cell culture

622 The breast cancer cell lines MCF-7 and MDA-MB-231 expressing tdTomato or eGFP were

623 produced by lentiviral transduction of cells originally obtained under MTA from NCI as part of

624 the NCI-60 panel. These cell lines were maintained in high glucose DMEM (MCF-7

625 tdTomato; Life Technologies, 21969-035) or phenol red free RPMI (MDA-MB-231 tdTomato

626 and MCF-7 eGFP; Sigma, D5671) with 10 % foetal bovine serum (Life Technologies, 10500-

627 064), 1 % L-glutamine (Life Technologies, 25030-024). To maintain the tdTomato protein

628 expression, the medium was supplemented with Puromycin (Gibco, A11138-03) at 1:1000

629 every passage (MCF-7 tdTomato) or every 3 weeks at 1:500 (MCF-7 eGFP) or 1:250 (MDA-

630 MB-231 tdTomato). Cells were maintained at 37 °C and 5 % CO_2 in a humidified atmosphere

631 during cell culture and measurements on the OptoRheo. All cell lines were subjected to

632 monthly mycoplasma testing and none of the lines used in this study tested positive at any

633 point.

634

Peptide gel precursor preparation

636 The precursor and gel preparation method was followed as previously published [57]. A

637 commercially available peptide preparation in powder form was used as the source of the

638 octapeptide gelator (Pepceuticals UK, FEFEFKFK, Phe-Glu-Phe-Glu-Phe-Lys-Phe-Lys). To

639 form the precursor, a mass of 10 mg peptide preparation was dissolved in 800 µL sterile

640 water (Sigma, W3500), using a 3 min vortex step followed by centrifugation (3 min at 1000

641 rpm) and a 2 hour incubation at 80 °C. After incubation, 0.5 M NaOH (Sigma, S2770) was

642 added incrementally to the gel until optically clear. The gel was vortexed, buffered by

643 addition of 100 µL 10x PBS (Gibco, 70011), and incubated at 80 °C overnight. The resulting

644 precursor could be stored at 4 °C until required.

645

646   Peptide gel formation with collagen I supplementation

647   Prior to peptide gel formation, the precursor was heated at 80 °C until liquid to ensure

648   homogeneity, before transferring to a 37 °C water bath. Cy5 labelled (in-house preparation,

649   see method below) rat tail Collagen I was neutralised directly before use with 1 M NaOH

650   according to manufacturer instructions, and diluted with sterile water and 10x PBS to a

651   concentration of 1 mg/ mL while keeping on ice at all times to prevent polymerisation.

652   Peptide gel formation was then induced by pH neutralisation on addition of cell culture

653   medium (with or without cell suspension) to the gel precursor. A final volume of 1.25 mL was

654   obtained from a preparation by adding 125 µL of cell suspension and 125 µL Cy5 collagen I

655   to a precursor volume of 1 mL. The end concentration of peptide preparation was 8 mg/ mL

656   and collagen I concentration was 100 µg/ mL. Polystyrene microspheres (Polybead®

657   Microspheres 6.00 µm; PolySciences) were added at final density of approx. 3×10^5

658   particles/ mL. The medium / cell suspension was thoroughly mixed with the precursor and

659   Collagen-I by gentle (reverse) pipetting, before plating at 100 µL per well into a 4 µ-well

660   glass bottom chambered coverslips (IBIDI, 80427) pre-mounted with a beamspliter cube

661   (ThorLabs, BS070). The wells were then flooded with cell culture medium and incubated at

662   37 °C and 5 % CO_2 in a humidified atmosphere. Sequential media changes (at least two)

663   over the next 2 hours ensured complete neutralisation and therefore gelation.

664

665   For cell encapsulation, the 125 µL volume of cell culture medium was prepared as a cell

666   suspension at 10x the intended final seeding density, to allow for the dilution factor on mixing

667   with the gel precursor. Trypsin-EDTA (0.25%; Life Technologies, 25200056) was used to

668   detach cells from 2D culture at sub-confluence. 1.25×10^5 cells were re-suspended in 125

669   µL cell culture medium, giving final seeding density in the peptide gel 1×10^5 cells/ mL. For

670   data in Figure 2B, a co-culture of MCF-7 (eGFP) and MDA-MB-231 (tdTomato) were at a

671   final seeding density of 1×10^6 cells/ mL for each cell type. 24 hrs post encapsulation culture

672   medium was replenished, with the addition of HEPES buffer (Life Technologies, 15630-056)

673   at 10 mM final concentration and 0.5 - 1 % penicillin/ streptomycin (Gibco, 15140122).

674

675   Prior to casting the gel, the beam splitter cubes were sterilised in absolute ethanol. Cubes

676   were soaked for 1 hour, then left to dry on a paper tissue inside the class 2 safety cabinet.

677   To minimise movement and consequently damage to delicate structure of a hydrogel, the

678   cubes were secured in place with glass coverslips.

679

680   Collagen labelling with Cy5

681   Rat tail collagen type 1 solution (10 mL; Gibco, A1048301) was mixed with 0.1 M sodium

682   bicarbonate buffer (10 mL, pH 8.5) and 110 µL Cy5 NHS ester solution (10 mg/ mL, DMSO)

683   added. The reaction mixture was stirred at 4 °C overnight. The reaction mixture was purified

684   via the dialysis method at 4 °C to remove the unreacted dye and yield the Cy5 labelled

685   collagen. It was then lyophilised and reconstituted in 20 mM acetic acid buffer.

686

687   Spheroid preparation

688   Corning 7007 Ultra-low attachment (ULA) 96-well round-bottom plates were used to culture

689   the 3D spheroids. 80 % confluent tdTomato MCF-7 monolayer cells were detached,

690   collected and the cell number determined using an automated cell counter (Biorad TC20). A

691   single-cell suspension was diluted in culture medium and cells seeded at 6000 cells/ well to

692   generate the spheroids (final volume of cell suspension in each well was 100 µL). The plates

693   were then centrifuged at 300 RCF for 5 min and cultured for 3 days until visible spheroid

694   formation.

695

696   For experiments on the OptoRheo, spheroids were placed in 4 µ-well glass bottom

697   chambered coverslips (IBIDI, 80427) using a P1000 pipette with the pipette tip cut off at the

698   end. Each spheroid was placed alone in 500 µL of phenol red-free culture media (1:1

699   DMEM:F12 supplemented with 10% FBS), ~ 5 mm away from the edge of a 10 mm beam

700   splitter cube (ThorLabs, BS070) (Fig S1A) in each well to enable LSFM imaging. Similar to

701   the peptide gel sample preparation protocol, beam splitter cubes were sterilised between

702   uses and secured in place in the chambered coverslips by wedging glass coverslips

703   between the cube and the chamber side wall.

704

705   Time lapse experiment

706   Time lapse videos were generated of MDA-MB231 cells expressing tdTomato fluorescent

707   protein seeded in peptide gel and supplemented with unlabelled collagen type I (Gibco,

708   A1048301) and bead probes (Polybead® Microspheres 6.00 µm; PolySciences). TrypLE

709   (Gibco, 12604) was used to detach cells from 2D culture at sub-confluence. The gels were

710   prepared in ibidi 4-well chambered coverslips with a beam splitter cube inserted at one end,

711   similar to the gel rheology experiments described above but with final cell seeding density

712   increased to 2×10^6 cells/ mL for video VS1 and 1×10^6 cells/ mL for video VS2, collagen I

713   increased to 150 µg/ mL and bead density increased to 3×10^5 / mL for samples in both

714   videos. The samples were kept at 37 °C and supplied with humidified 5 % CO_2 using cell

715   culture incubators prior to imaging and then the Okolab stage-top incubator during the

716   experiment.

717

718   Single channel image volumes were acquired at 10 minute time intervals with light sheet

719   illumination at 532 nm using an automated LabVIEW program on the OptoRheo. Acquired

720   image volumes were subjected to 3D deconvolution using the Wiener Filter Preconditioned

721   Landweber (WPL) method in the Parallel Iterative Deconvolution plugin in Fiji. The 4D videos

722   were rendered in Imaris (10.0.0, Oxford Instruments).

723

724   The time lapse videos were halted at regular intervals to acquire microrheology

725   measurements within the same field of view by recording the Brownian motion of 6 μm bead

726   probes at 5 kHz for 1.5 x 10^6 frames. The bead trajectories were analysed as described in

727   the microrheology section above and depicted as spheres (to scale) in the videos by creating

728   volume objects in a separate colour channel with a colour shade corresponding to the local

729   measurement at the time.

730

References

732   1. Discher, D. E., Janmey, P. & Wang, Y. Tissue Cells Feel and Respond to the Stiffness of

733   Their Substrate. *Science* **310**, 1139–1143 (2005).

734   2. Lo, C. M., Wang, H. B., Dembo, M. & Wang, Y. L. Cell movement is guided by the

735   rigidity of the substrate. *Biophys J* **79**, 144–152 (2000).

736   3. Pelham, R. J. & Wang, Y. Cell locomotion and focal adhesions are regulated by substrate

737   flexibility. *PNAS* **94**, 13661–13665 (1997).

738   4. Veenvliet, J. V., Lenne, P.-F., Turner, D. A., Nachman, I. & Trivedi, V. Sculpting with

739   stem cells: how models of embryo development take shape. *Development* **148**,

740   dev192914 (2021).

741   5. Fernandez, P. & Bausch, A. R. The compaction of gels by cells: a case of collective

742   mechanical activity. *Integrative Biology* **1**, 252–259 (2009).

743   6. Bloom, R. J., George, J. P., Celedon, A., Sun, S. X. & Wirtz, D. Mapping Local Matrix

744   Remodeling Induced by a Migrating Tumor Cell Using Three-Dimensional Multiple-

745   Particle Tracking. *Biophysical Journal* **95**, 4077–4088 (2008).

746   7. Lu, P., Weaver, V. M. & Werb, Z. The extracellular matrix: A dynamic niche in cancer

747   progression. *Journal of Cell Biology* **196**, 395–406 (2012).

748   8. Long, Y., Niu, Y., Liang, K. & Du, Y. Mechanical communication in fibrosis

749   progression. *Trends in Cell Biology* **32**, 70–90 (2022).

750   9.   Meng, H. & Nel, A. E. Use of Nano Engineered Approaches to Overcome the Stromal

751   Barrier in Pancreatic Cancer. *Adv Drug Deliv Rev* **130**, 50–57 (2018).

752   10. Piersma, B., Hayward, M. K. & Weaver, V. M. Fibrosis and cancer: A strained

753   relationship. *Biochim Biophys Acta Rev Cancer* **1873**, 188356 (2020).

754   11. Gong, Z. *et al.* Matching material and cellular timescales maximizes cell spreading on

755   viscoelastic substrates. *PNAS* **115**, E2686–E2695 (2018).

756   12. Ashworth, J. C. *et al.* Peptide gels of fully-defined composition and mechanics for

757   probing cell-cell and cell-matrix interactions in vitro. *Matrix Biology* **85–86**, 15–33

758   (2019).

759   13. Chaudhuri, O. Viscoelastic hydrogels for 3D cell culture. *Biomaterials Science* **5**, 1480–

760   1490 (2017).

761   14. Chaudhuri, O., Cooper-White, J., Janmey, P. A., Mooney, D. J. & Shenoy, V. B. Effects

762   of extracellular matrix viscoelasticity on cellular behaviour. *Nature* **584**, 535–546 (2020).

763   15. Charrier, E. E., Pogoda, K., Wells, R. G. & Janmey, P. A. Control of cell morphology

764   and differentiation by substrates with independently tunable elasticity and viscous

765   dissipation. *Nat Commun* **9**, 449 (2018).

766   16. Greiss, F., Deligiannaki, M., Jung, C., Gaul, U. & Braun, D. Single-Molecule Imaging in

767   Living Drosophila Embryos with Reflected Light-Sheet Microscopy. *Biophysical Journal*

768   **110**, 939–946 (2016).

769   17. Beicker, K., O'Brien, E. T., Falvo, M. R. & Superfine, R. Vertical Light Sheet Enhanced

770   Side-View Imaging for AFM Cell Mechanics Studies. *Scientific Reports* **8**, 1504 (2018).

771   18. Kashekodi, A. B., Meinert, T., Michiels, R. & Rohrbach, A. Miniature scanning light-

772   sheet illumination implemented in a conventional microscope. *Biomedical Optics Express*

773   **9**, 4263 (2018).

33

774   19. Gustavsson, A. K., Petrov, P. N., Lee, M. Y., Shechtman, Y. & Moerner, W. E. 3D

775   single-molecule super-resolution microscopy with a tilted light sheet. *Nature*

776   *Communications* **9**, 123 (2018).

777   20. Buchmann, B. *et al.* Mechanical plasticity of collagen directs branch elongation in human

778   mammary gland organoids. *Nature Communications* **12**, 2759 (2021).

779   21. Hafner, J. *et al.* Monitoring matrix remodeling in the cellular microenvironment using

780   microrheology for complex cellular systems. *Acta Biomaterialia* **111**, 254–266 (2020).

781   22. Ciccone, G. *et al.* What Caging Force Cells Feel in 3D Hydrogels: A Rheological

782   Perspective. *Advanced Healthcare Materials* **9**, 2000517 (2020).

783   23. Han, Y. L. *et al.* Cell swelling, softening and invasion in a three-dimensional breast

784   cancer model. *Nature Physics* **16**, 101–108 (2020).

785   24. Guadayol, Ò. *et al.* Microrheology reveals microscale viscosity gradients in planktonic

786   systems. *PNAS* **118**, e2011389118 (2021).

787   25. Matheson, A. B. *et al.* Optical Tweezers with Integrated Multiplane Microscopy

788   (OpTIMuM): a new tool for 3D microrheology. *Scientific Reports* **11**, 5614 (2021).

789   26. Huisken, J., Swoger, J., Del Bene, F., Wittbrodt, J. & Stelzer, E. H. K. Optical Sectioning

790   Deep Inside Live Embryos by Selective Plane Illumination Microscopy. *Science* **305**,

791   1007–1009 (2004).

792   27. Pitrone, P. G. *et al.* OpenSPIM: an open-access light-sheet microscopy platform. *Nature*

793   *methods* **10**, 598–599 (2013).

794   28. Reynaud, E. G., Krzic, U., Greger, K. & Stelzer, E. H. K. Light sheet-based fluorescence

795   microscopy: more dimensions, more photons, and less photodamage. *HFSP journal* **2**,

796   266–75 (2008).

797   29. Hu, Y. S. *et al.* Light-sheet Bayesian microscopy enables deep-cell super-resolution

798   imaging of heterochromatin in live human embryonic stem cells. *Optical Nanoscopy* **2**, 7

799   (2013).

800   30. Gebhardt, J. C. M. *et al.* Single-molecule imaging of transcription factor binding to DNA

801   in live mammalian cells. *Nature Methods* **10**, 421–426 (2013).

802   31. Tassieri, M. Microrheology with optical tweezers: peaks & troughs. *Current Opinion in*

803   *Colloid and Interface Science* **43**, 39–51 (2019).

804   32. Lee, M. P., Padgett, M. J., Phillips, D., Gibson, G. M. & Tassieri, M. Dynamic stereo

805   microscopy for studying particle sedimentation. *Optics Express* **22**, 4671 (2014).

806   33. Blanchard, P. M. & Greenaway, A. H. Simultaneous multiplane imaging with a distorted

807   diffraction grating. *Appl. Opt.* **38**, 6692 (1999).

808   34. Dasgupta, R., Verma, R. S., Ahlawat, S., Chaturvedi, D. & Gupta, P. K. Long-distance

809   axial trapping with Laguerre–Gaussian beams. *Appl. Opt., AO* **50**, 1469–1476 (2011).

810   35. Tassieri, M. *et al.* Microrheology with Optical Tweezers: Measuring the relative viscosity

811   of solutions 'at a glance'. *Scientific Reports* **5**, 8831 (2015).

812   36. Pal, A. *et al.* A 3D Heterotypic Breast Cancer Model Demonstrates a Role for

813   Mesenchymal Stem Cells in Driving a Proliferative and Invasive Phenotype. *Cancers* **12**,

814   2290 (2020).

815   37. Vasudevan, J., Lim, C. T. & Fernandez, J. G. Cell Migration and Breast Cancer

816   Metastasis in Biomimetic Extracellular Matrices with Independently Tunable Stiffness.

817   *Advanced Functional Materials* **30**, 2005383 (2020).

818   38. Lovitt, C. J., Shelper, T. B. & Avery, V. M. Doxorubicin resistance in breast cancer cells

819   is mediated by extracellular matrix proteins. *BMC Cancer* **18**, 41 (2018).

820   39. Shin, M. *et al.* Rheological criteria for distinguishing self-healing and non-self-healing

821   hydrogels. *Polymer* **229**, 123969 (2021).

822   40. Abidine, Y. *et al.* Physical properties of polyacrylamide gels probed by AFM and

823   rheology. *EPL* **109**, 38003 (2015).

824   41. Cai, P. C. *et al.* Rheological Characterization and Theoretical Modeling Establish

825   Molecular Design Rules for Tailored Dynamically Associating Polymers. *ACS Cent. Sci.*

826   **8**, 1318–1327 (2022).

827   42. Leach, J. *et al.* Comparison of Faxén's correction for a microsphere translating or rotating

828   near a surface. *Physical Review E* **79**, 026301 (2009).

829   43. Meza, J. M. H. *et al.* Particle/wall electroviscous effects at the micron scale: comparison

830   between experiments, analytical and numerical models. *J. Phys.: Condens. Matter* **34**,

831   094001 (2021).

832   44. Prevedel, R., Diz-Muñoz, A., Ruocco, G. & Antonacci, G. Brillouin microscopy: an

833   emerging tool for mechanobiology. *Nat Methods* **16**, 969–977 (2019).

834   45. Rohrbach, A., Tischer, C., Neumayer, D., Florin, E.-L. & Stelzer, E. H. K. Trapping and

835   tracking a local probe with a photonic force microscope. *Review of Scientific Instruments*

836   **75**, 2197–2210 (2004).

837   46. Jünger, F. *et al.* Measuring Local Viscosities near Plasma Membranes of Living Cells

838   with Photonic Force Microscopy. *Biophysical Journal* **109**, 869–882 (2015).

839   47. Gjorevski N. *et al.* Tissue geometry drives deterministic organoid patterning. *Science*

840   **375**, eaaw9021 (2022).

841   48. Schindelin, J. *et al.* Fiji: an open-source platform for biological-image analysis. *Nature*

842   *methods* **9**, 676–82 (2012).

843   49. Hörl, D. *et al.* BigStitcher: reconstructing high-resolution image datasets of cleared and

844   expanded samples. *Nat Methods* **16**, 870–874 (2019).

845   50. Wan, Y. *et al.* FluoRender: joint freehand segmentation and visualization for many-

846   channel fluorescence data analysis. *BMC Bioinformatics* **18**, 280 (2017).

847   50. Frisch, D. point2trimesh () - distance between point and triangulated surface.

848   (https://www.mathworks.com/matlabcentral/fileexchange/52882-point2trimesh-distance-

849   between-point-and-triangulated-surface), MATLAB Central File Exchange (2016).

850   Retrieved December 1, 2021.

851   52. Dalgarno, P. A. *et al.* Multiplane imaging and three dimensional nanoscale particle

852   tracking in biological microscopy. *Optics Express* **18**, 877 (2010).

853   53. Edelstein, A., Amodaj, N., Hoover, K., Vale, R. & Stuurman, N. Computer Control of

854   Microscopes Using µManager. *Current Protocols in Molecular Biology* **92**, 14.20.1-

855   14.20.17 (2010).

856   54. Tassieri, M., Evans, R. M. L., Warren, R. L., Bailey, N. J. & Cooper, J. M.

857   Microrheology with optical tweezers: Data analysis. *New Journal of Physics* **14**, 115032

858   (2012).

859   55. Smith, M. G., Gibson, G. M. & Tassieri, M. i-RheoFT: Fourier transforming sampled

860   functions without artefacts. *Sci Rep* **11**, 24047 (2021).

861   56. Matheson, A. B. *et al.* Microrheology With an Anisotropic Optical Trap. *Front. Phys* **9**,

862   621512 (2021).

863   57. Ashworth, J. C. *et al.* Preparation of a User-Defined Peptide Gel for Controlled 3D

864   Culture Models of Cancer and Disease. *J Vis Exp* e61710 (2020) doi:10.3791/61710.

865

866   **Acknowledgements**

871

872   The MCF-7 eGFP, MCF7-tdTomato and MDA-MB-231 tdTomato cell lines were provided by

873   and with thanks to Prof. Anna Grabowska, University of Nottingham.

874

875   **Competing Interests**
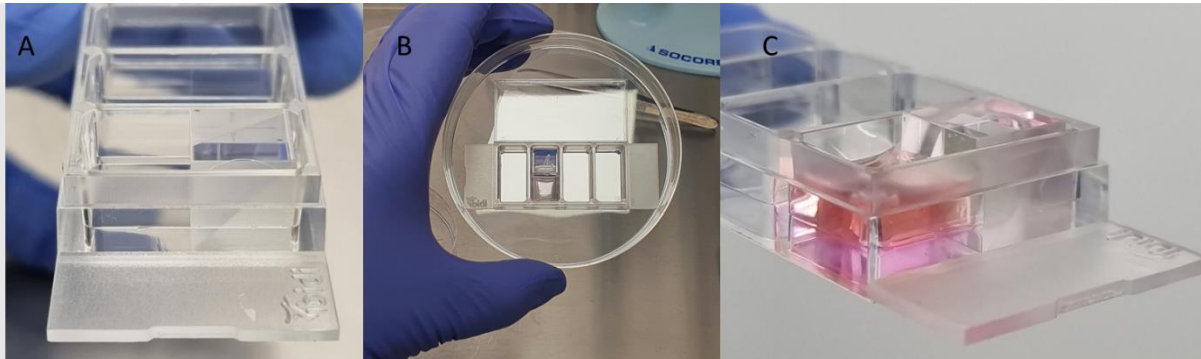
876   The authors declare no conflicts of interest.

877

878

879 **Supplementary Information**

880

881   1.   Sample preparation

883   Fig S1: Sample set up: A. Side view of the 4 µ-well chambered coverslip with a 10 mm

884   beam splitter cube inserted with the reflective surface facing the empty half of the chamber.

885   B. Top view of a sample with the gel cast next to the beam splitter cube. C. Side view of the

886   peptide hydrogel topped up with medium next to the beam splitter cube.

887

888   2.   Light sheet properties
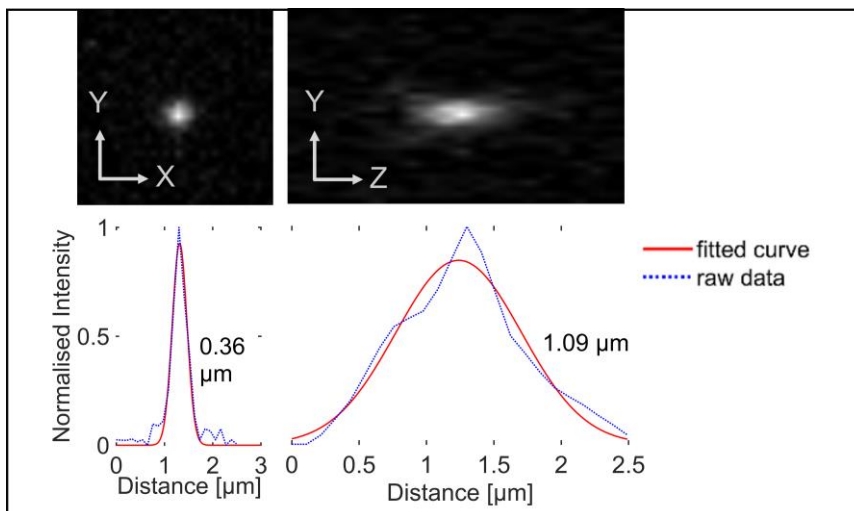
890

891   Fig S2: Lateral (left) and axial (right) point spread functions (PSFs) of the system along the

892   XY (0.36 µm FWHM) and YZ (1.09 µm FWHM) planes measured using fluorescent sub-

893   diffraction sized microspheres (diameter = 200 nm, λ_{ex} / λ_{em} = 532 nm / 580 nm) at ~200 μm

894   from the coverslip.

895

896   Supplementary videos:

897

898   VS1: **MDA-MB-231 (tdTomato) cells changing morphology** in 3D within a hydrogel

899   matrix supplemented with collagen I (unlabelled). The video was acquired over ~7 hours with

900   a 10 min time interval between frames. Changes in ECM rheology and cell morphology

901   appear related as a more compliant gel at the start of the video (see table S1 below)

902   precedes cell elongation while an increase in stiffness around 6 hours into the experiment

903   corresponds with a retracted cell morphology.

904

Time	Measurement location 1 (G_0' [Pa])	Measurement location 2 (G_0' [Pa])	Measurement location 3 (G_0' [Pa])
0 min	2.3×10^{-2}	2.0×10^{-2}	1.5×10^{-2}
120 min	1.5×10^{-2}	0.7×10^{-2}	0.4×10^{-2}
240 min	1.2×10^{-2}	2.2×10^{-2}	3.2×10^{-2}
360 min	20.2×10^{-2}	22.9×10^{-2}	24.0×10^{-2}

905   Table S1: Microrheology measurements depicted in supplementary video VS1 clockwise

906   from bottom over the time course of the experiment.

907

908   VS2: **MDA-MB-231 (tdTomato) cells migrating** in 3D within a hydrogel matrix

909   supplemented with collagen I (unlabelled). The video was acquired over 4 hours with a 10

910   min time interval between frames. Rheology measurements showed a more compliant

911   region (2×10^{-2} Pa) near (~ 50 μm) the migratory path depicted as a dark pink sphere as

912   opposed to farther away (6×10^{-2} Pa at ~80 μm away) depicted as a bright pink sphere.

913